

## Electric-field-controlled antiferromagnetic domains in epitaxial BiFeO<sub>3</sub> thin films probed by neutron diffraction

W. Ratcliff II,<sup>1,\*</sup> Zahra Yamani,<sup>2</sup> V. Anbusathaiah,<sup>3,†</sup> T. R. Gao,<sup>3</sup> P. A. Kienzle,<sup>1</sup> H. Cao,<sup>4</sup> and I. Takeuchi<sup>3</sup>

<sup>1</sup>NIST Center for Neutron Research, National Institute of Standards and Technology, Gaithersburg, Maryland 20899, USA

<sup>2</sup>Canadian Neutron Beam Centre, National Research Council, Chalk River Laboratories, Chalk River, Ontario, Canada K0J 1J0

<sup>3</sup>Department of Materials Science and Engineering, University of Maryland, College Park, Maryland 20424, USA

<sup>4</sup>Quantum Condensed Matter Division, Oak Ridge National Laboratory, Oak Ridge, Tennessee 37831, USA

(Received 10 October 2012; revised manuscript received 4 February 2013; published 15 April 2013)

Direct evidence of controlling the population of magnetic domains in BiFeO<sub>3</sub> thin films through electric field is reported using neutron diffraction. By fabricating BiFeO<sub>3</sub> thin films on vicinal SrTiO<sub>3</sub> substrates, we have achieved ferroelectric monodomains as confirmed by piezoresponse force microscopy. The application of an electric field between the bottom SrRuO<sub>3</sub> and the top electrode switches the ferroelectric domain state with concomitant changes in magnetic reflections observed with neutron diffraction, indicating changes in the antiferromagnetic domain populations. The observed magnetoelectric switching behavior by neutron diffraction is compared with the electric-field effect on the magneto-optical Kerr effect measurement on patterned pads of exchange coupled Co film deposited on top of the BiFeO<sub>3</sub> films. The present result shows possible new directions for the realization of magnetoelectric devices.

DOI: [10.1103/PhysRevB.87.140405](https://doi.org/10.1103/PhysRevB.87.140405)

PACS number(s): 77.55.Nv, 61.05.fm, 75.85.+t

The magnetoelectric effect in BiFeO<sub>3</sub> (BFO) has previously been investigated through direct imaging with photoemission-electron-microscopy and exchange coupling with an upper ferromagnetic layer.<sup>1–5</sup> However, investigating antiferromagnetic (AFM) domains in BFO is challenging. In single-crystal BFO, changes in AFM domains as electric field is applied have been observed by neutron diffraction.<sup>6,7</sup> However, because device applications require BFO thin films—which can have markedly different domain structures than single crystals<sup>8–10</sup>—the electric-field effect in thin films must be investigated directly. Here, we used neutron diffraction to demonstrate electric-field-induced modulation of AFM domain populations in epitaxial BFO thin films. Co/BFO thin-film multilayers showed electric-field-tunable exchange coupling attributable to the domain-population modulation.

It is known that even subtle modification of microstructure can profoundly affect the magnetic structure in epitaxial BFO thin films.<sup>9</sup> Thus, choosing the right BFO structure is imperative. Single-ferroelectric-domain BFO films can be grown on vicinal substrates,<sup>11</sup> which simplifies the investigation of its behavior.<sup>9,10</sup> Here, we deposited 1- $\mu\text{m}$  epitaxial BFO films at 590 °C and 25 mT oxygen partial pressure by pulsed laser deposition on 50-nm SrRuO<sub>3</sub> (SRO) -buffered (bottom electrode) (001)-oriented SrTiO<sub>3</sub> (STO) substrates with a 4° miscut along the [110] direction. The epitaxial relationship between the film and the substrate were determined through the use of x-ray reciprocal space maps.

By using a conventional piezoresponse force microscopy (PFM; Pt/Ir-coated cantilever, scanning along the [110] direction of the substrate), we characterized the films' ferroelectric domain structures. An ac signal [ $V_{ac} = V_0 \sin(2\pi ft)$ ]; amplitude,  $V_0 = 3 V_{\text{peak-peak}}$  and frequency,  $f = 7$  kHz) was applied between the cantilever and bottom electrode to image the out-of plane and in-plane components of the ferroelectrics with the aid of two lock-in amplifiers.

The as-deposited BFO film showed step flow growth along the miscut direction [110] and a smooth surface (rms roughness

$\approx 1.7$  nm) [Fig. 1(a)]. No piezoresponse contrast in the out-of-plane or in-plane direction was observed [Figs. 1(b) and 1(c)], confirming the monodomain ferroelectric structure.<sup>11</sup> Next, we prepared the film for electric-field-dependent neutron diffraction without compromising the geometry or volume.

To avoid dielectric breakdown due to defects and pinholes over the  $10 \times 10$  mm<sup>2</sup> surface area necessary for neutron diffraction, we fabricated two samples [S1 and S2; Fig. 1(d)]. A Pd top-electrode layer (100 nm) was sputtered on the BFO/SRO/STO epitaxial multilayer, and a  $40 \times 40$  array of  $100 \times 100$   $\mu\text{m}^2$  electrode patterns was generated on the Pd surface by photolithography. The multilayer was then patterned down to the SRO layer by ion-beam etching to create a Pd/BFO/SRO capacitor pillar array, ensuring that BFO was removed to 90% from film regions where the electric field would *not* be applied. We determined the electric coercive field from the polarization versus electric field hysteresis loop using a probe station equipped with a Radiant Precision II analyzer<sup>12</sup> to determine the switching bias voltage for neutron diffraction [Fig. 1(e)]. After checking the capacitor pillars for electrical insulation (up to 70% of pillars maintained sufficient electrical insulation) using the PE analyzer, we wired all the nonshorted capacitors together in groups.

Neutron diffraction was performed on a triple-axis spectrometer equipped with an Eulerian cradle (BT-9, NIST Center for Neutron Research), a four-circle single-crystal diffractometer (HB-3A, High Flux Isotope Reactor, Oak Ridge National Laboratory),<sup>13</sup> and N5 and C5 triple-axis spectrometers (Chalk River). The BT-9 horizontal collimations before and after the monochromator were 40' and 10', respectively. Before and after the analyzer, they were 40' and 200'. There was a pyrolytic graphite (PG) analyzer and PG filters before and after the sample to remove  $\lambda/2$  contamination. Due to strong scattering from the substrate, the peak position was aligned on reflections from the substrate rather than the film; thus all coordinates are expressed using the substrate lattice constants. Experiments on N5 were performed using an Eulerian cradle with a PG

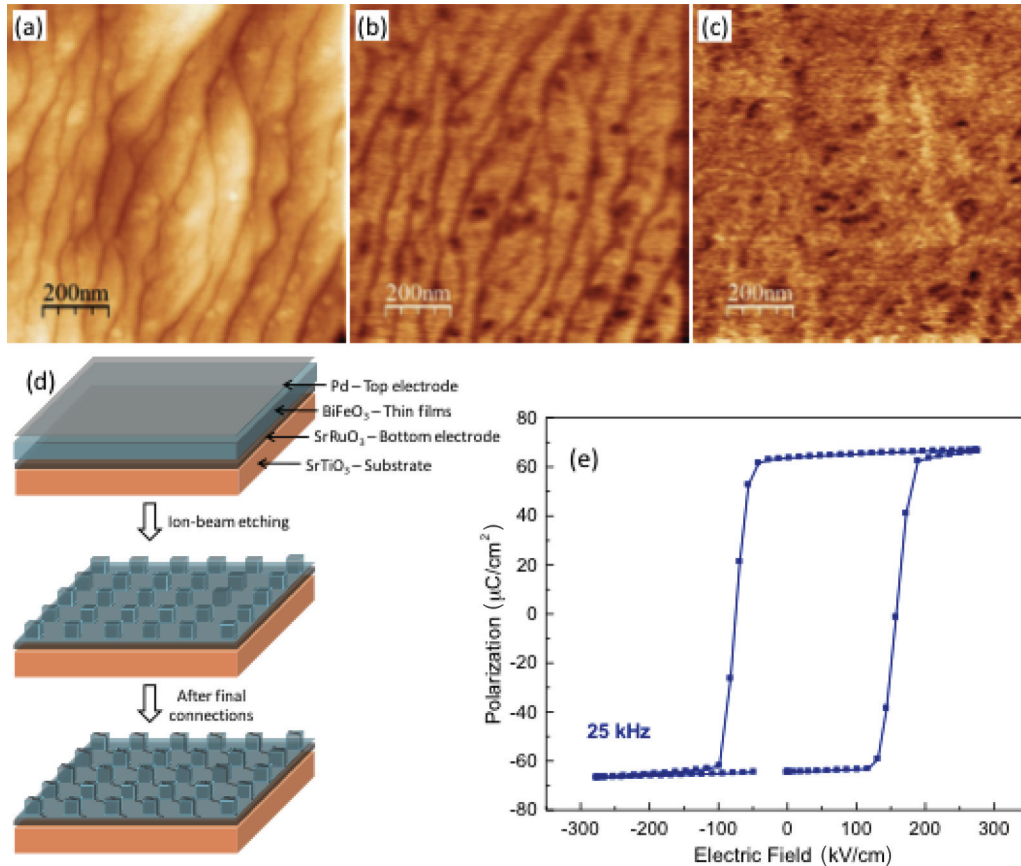


FIG. 1. (Color online) (a) Topography, (b) out-of-plane, and (c) in-plane PFM images of as-grown BFO thin films. (d) Fabrication of Pd/BFO/SRO microcapacitors. (e) Polarization versus electric field hysteresis loop measured at a capacitor.

monochromator and analyzer ( $E_f = E_i = 14.56$  meV). Collimations were set to  $0.8^\circ$  and  $0.55^\circ$  before and after the sample, respectively, and open before the monochromator and after the analyzer. A PG filter after the sample removed higher-order contamination from the neutron beam. Polarized neutron scattering was performed on the C5 spectrometer. The neutron beams were polarized with Heusler (111) crystals as monochromator and analyzer ( $E_f = 14.56$  meV). Permanent magnet guide fields maintained neutron polarization in the incident and scattered beam channels. Two PG filters after the sample eliminated higher-order contamination from the beam. Mezei flippers before and after the sample allowed measurement of all four scattering cross sections ( $I^{++}$ ,  $I^{--}$ ,  $I^{+-}$ ,  $I^{-+}$ ). A five-coil Helmholtz assembly controlled the neutron spin orientation at the sample by producing an  $\sim 10$  G magnetic field. The magnetic field orientation at the sample was automatically adjusted to allow measurement of neutron spin perpendicular to the scattering plane and parallel to any orientation in that plane. The flipping ratio was measured as  $\sim 15:1$  for various field configurations.

In our setup [Fig. 2(a)], the ferroelectric polarization vector was directed along the [111] direction. Because the film was nominally rhombohedral (with slight monoclinic distortion<sup>14</sup>), the [111] was a threefold axis with three magnetic propagation vectors:  $\vec{k}_1 = (\delta\delta 0)$ ,  $\vec{k}_2 = (\delta 0\delta)$ , and  $\vec{k}_3 = (0\delta\delta)$  [Fig. 2(a), red arrows].<sup>15</sup> The domain populations in BFO thin films<sup>9,10</sup> and single crystals<sup>6,7,16</sup> depend on electric-field strength,

strain, and sample preparation. Reflections from each domain are shown in Fig. 2(a) (black ovals). When we applied an electric field, the ferroelectric polarization switches from the [111] direction to the [11-1] direction because it has only one polarization variant; the propagation vector plane also switches

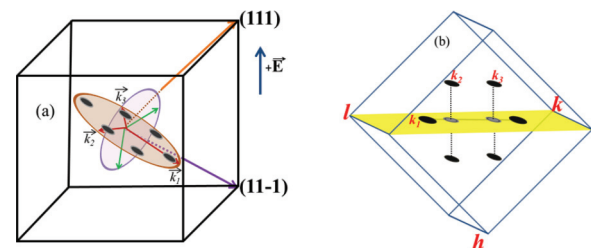


FIG. 2. (Color online) (a) Applied electric-field direction, ferroelectric polarization directions (orange and violet arrows corresponding to positive and negative electric fields, respectively), and planes containing three equivalent magnetic modulation vectors perpendicular to the polarization vector (orange and violet ellipses). Black ovals indicate magnetic reflections from the three magnetic domains. (b) Magnetic reflections due to the in-plane domain and the projections of the out-of-plane domains onto an  $\{hkk\}$ -type plane: black ovals in yellow plane, reflections from the in-plane domain ( $k_1$ ); gray ovals, projections of the reflections from the out-of-plane domains ( $k_2$  and  $k_3$ ).

to remain normal to the polarization. One propagation vector is unchanged by field switching.

Figure 2(b) shows the six possible reflections: two in the scattering plane and two each above and below the plane. On a triple-axis spectrometer, measurements are performed in a scattering plane defined by the detector and the monochromator. Because instrumental resolution in the out-of-plane direction is broad, we capture the projections of the two out-of-plane magnetic domains [Fig. 2(b)]. Thus, the peak intensity and its profile are due to in-plane and (projected) out-of-plane domains. In single-crystal studies, domain populations were determined by fits to line scans performed in multiple scattering planes<sup>6,16</sup> or were observed directly.<sup>5</sup> Changing the relative population of the domains affects the intensities and profiles of the in-plane peaks: The peak centers move closer together or farther apart. Thus, any change in the domain population should change the peak separation.

We surveyed the domain populations in S1 in the poled state ( $-20$  V) on HB-3A and N5 at Chalk River. The film was mounted in the zone defined by the (111) and (1 - 10) reflections. The reciprocal space map [Fig. 3(a)] showed two peaks, indicating an incommensurate structure with a periodicity comparable to that of single-crystal samples. A  $\psi$  scan through the center of the two reflections [Fig. 3(b)]

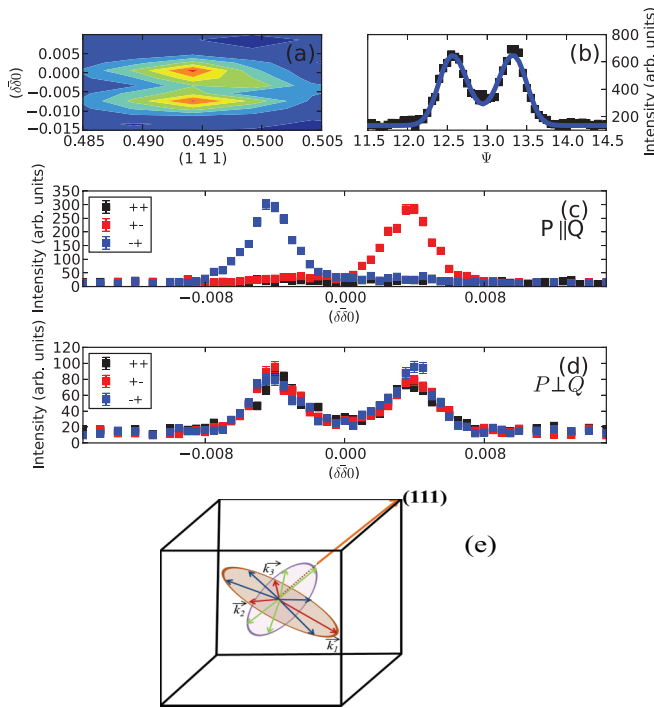


FIG. 3. (Color online) (a) Contour map of the neutron diffraction in the  $[hk h+k/2]$  zone for S2 about the (0.5 0.5 05) position in reciprocal space after application of  $-200$  kV/cm. (b)  $\psi$  cut through the two peaks (fits described in text). Spin Flip (SF) and Non Spin Flip (NSF) cross sections for (c)  $P \parallel Q$  and (d)  $P \perp Q$  about the (0.5 0.5 0.5) position. (e) Magnetic structure: red arrows, propagation wave vectors for the three possible magnetic domains; red plane, plane of spiral; blue arrows, moments in this plane; purple plane, plane of spiral for single crystals (for domain defined by  $\vec{k}_3$  propagation vector); and green arrows, moments in this plane. Error bars =  $+/- 1\sigma$ .

was carefully fitted to

$$I = A_1 \frac{1}{\sigma \sqrt{2\pi}} e^{-[(\psi - \psi_0 - \psi_c)^2 / 2\sigma^2]} + A_1 \frac{1}{\sigma \sqrt{2\pi}} e^{-[(\psi + \psi_0 - \psi_c)^2 / 2\sigma^2]} + A_2 \frac{1}{\sigma \sqrt{2\pi}} e^{-[\psi - (\psi_0/2) - \psi_c]^2 / 2\sigma^2} + A_2 \frac{1}{\sigma \sqrt{2\pi}} e^{-[(\psi + (\psi_0/2) - \psi_c)^2 / 2\sigma^2]}$$

in which the widths were the same (the instrumental resolution should be approximately constant in this range), and the center and amplitudes were allowed to vary. The reflection positions relative to the center ( $\psi_c$ ) are characterized by one parameter ( $\psi_0$ ). Fitting to four peaks (rather than two) reduced the normalized  $\chi^2$  from 2.13 to 1.8. This is statistically significant, and our fit corresponds to an  $\sim 3:1$  in-plane/out-of-plane contribution ratio.

Next we performed polarized beam measurements on C5 at Chalk River. In polarized neutron diffraction, we can select the neutron spin state before scattering by the sample. After scattering, we can also select which spin state of the scattered neutrons to measure. Neglecting incoherent scattering, the polarized neutron diffraction cross section is described by<sup>17</sup>

$$\begin{aligned} \frac{d^2\sigma^{++}}{d\Omega d\omega} &= \frac{k_f}{k_i} [\langle NN^* \rangle_\omega + \hat{P} \cdot \langle N \vec{M}_\perp^* \rangle_\omega + \hat{P} \cdot \langle N^* \vec{M}_\perp \rangle_\omega \\ &\quad + \langle (\hat{P} \cdot \vec{M}_\perp) (\hat{P} \cdot \vec{M}_\perp^*) \rangle_\omega], \\ \frac{d^2\sigma^{--}}{d\Omega d\omega} &= \frac{k_f}{k_i} [\langle NN^* \rangle_\omega - \hat{P} \cdot \langle N \vec{M}_\perp^* \rangle_\omega - \hat{P} \cdot \langle N^* \vec{M}_\perp \rangle_\omega \\ &\quad + \langle (\hat{P} \cdot \vec{M}_\perp) (\hat{P} \cdot \vec{M}_\perp^*) \rangle_\omega] \\ \frac{d^2\sigma^{+-}}{d\Omega d\omega} &= \frac{k_f}{k_i} [\langle \vec{M}_\perp \vec{M}_\perp^* \rangle_\omega - \langle (\hat{P} \cdot \vec{M}_\perp) (\hat{P} \cdot \vec{M}_\perp^*) \rangle_\omega \\ &\quad - i \langle (\hat{P} \cdot (\vec{M}_\perp \wedge \vec{M}_\perp^*)) \rangle_\omega], \\ \frac{d^2\sigma^{-+}}{d\Omega d\omega} &= \frac{k_f}{k_i} [\langle \vec{M}_\perp \vec{M}_\perp^* \rangle_\omega - \langle (\hat{P} \cdot \vec{M}_\perp) (\hat{P} \cdot \vec{M}_\perp^*) \rangle_\omega \\ &\quad + i \langle (\hat{P} \cdot (\vec{M}_\perp \wedge \vec{M}_\perp^*)) \rangle_\omega], \end{aligned}$$

where  $k_i$  and  $k_f$  are incoming and outgoing neutron wave vectors,  $P$  is neutron polarization, and  $M$  is the sample moment direction. Nuclear scattering is contained in the  $N$  term. Neutron polarization is indicated by  $+/-$ .

We performed polarized beam measurements at the (0.5 0.5 0.5) position in the zone defined by the (111) and (1 - 10) reflections [Fig. 3(c)]. For  $P \parallel Q$  (0.5 0.5 0.5), splitting between the  $+/-$  and  $-/+$  cross sections was strong, consistent with a chirality axis along the [111] direction and magnetic moments in the plane normal to [111]. For  $P \perp Q$ , the two spin-flip cross sections gave the same intensity [Fig. 3(d)], also consistent with a chirality axis along [111]. Thus, we conclude that the magnetic structure of this BFO film differs markedly from that of the single crystal [Fig. 3(e)]. There is a cycloid with moments spiraling in the plane normal to the polarization, consistent with theoretical predictions of an easy plane in films.<sup>18</sup>

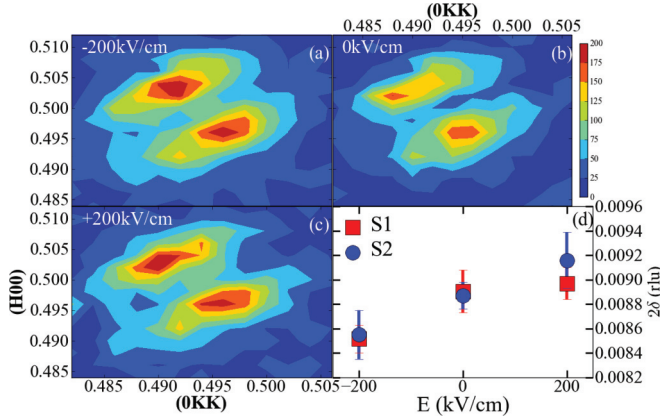


FIG. 4. (Color online) Contour maps of neutron diffraction in the  $[hkk]$  zone for S1 about the (0.5 0.5 05) position in reciprocal space. (d) Peak separation versus applied electric field for S1 and S2 (error bars =  $\pm 1\sigma$ ). The separation between the centers of the Gaussians fit to the observed peaks.

We performed neutron diffraction measurements on S2 in its unpoled state first. Then the sample was removed, a  $-200$  KV/cm electric field was applied to the parallel arrays of capacitor pillars along the film normal direction ( $[001]$ ), and the sample was remeasured. Finally, a  $+200$  KV/cm electric field was applied, and the sample was remeasured. The sample was carefully realigned each time in the same orientation on the spectrometer. S1 was also measured first in the unpoled state; then a  $+200$  KV/cm field was applied to the pillars along the film normal direction, the sample was measured, and a  $-200$  KV/cm field was applied.

We prepared a reciprocal space map of S1 measured in the  $[hkk]$  scattering plane for the unpoled state and after sequential application of  $+200$  and  $-200$  KV/cm fields (Fig. 4). Two two-dimensional Gaussians were fitted to the data from both samples [Fig. 4(d)]. The intensity of one Gaussian was parametrized by

$$I(x, y) = A \exp \left[ -\frac{1}{2} \left\{ \left( \frac{\cos^2 \theta}{\sigma_x^2} + \frac{\sin^2 \theta}{\sigma_y^2} \right) (x - x_0)^2 + \left( -\frac{\sin 2\theta}{2\sigma_x^2} + \frac{\sin 2\theta}{2\sigma_y^2} \right) (x - x_0)(y - y_0) + \left( \frac{\sin^2 \theta}{\sigma_x^2} + \frac{\cos^2 \theta}{\sigma_y^2} \right) (y - y_0)^2 \right\} \right],$$

where  $A$  is amplitude,  $\sigma_x$  and  $\sigma_y$  are standard deviations,  $\theta$  is the rotation angle of the Gaussian, and  $(x_0, y_0)$  is the center. We constrained the two Gaussians to the same width because the instrumental resolution was constant over the measured range. The peak separation ( $2\delta$ ) for the two samples varied similarly with the applied electric field, and the  $\delta$  values agreed with each other for the same applied field.

The data were fitted with DREAM,<sup>19</sup> a Markov chain Monte Carlo simulation method with differential evolution update steps. The resulting Markov chains converge to sampling from the underlying probability distribution; from this sample, the expected and maximum likelihood values can be estimated and their uncertainties accurately assessed. This method is powerful when the optimized parameters are

correlated and cannot be determined independently. We fitted the peak centers, separation, and amplitudes to estimate the electric-field effect on the peak separation. From these fits, we infer that the relative domain populations change with the applied field. That AFM domains could be electrically switched between population states in BFO thin films provides direct evidence that electric-field-tunable exchange bias can be established in ferromagnet/BFO bilayers, which will be the basis for electric-field-switchable magnetoresistance devices. Exchange coupling in ferromagnet/BFO systems has been reported, with single-crystal and thin-film BFO behaving differently.<sup>5,20,21</sup>

To study the effect of the field-induced AFM domain-population change on exchange coupling with a ferromagnetic layer, we prepared another  $1\text{-}\mu\text{m}$  epitaxial BFO film ( $4^\circ$  miscut along the  $[110]$  direction) and deposited a  $5\text{-nm}$  Co layer by electron beam evaporation at room temperature (with no magnetic field applied). (A  $5\text{-nm}$  Pt layer was deposited on the Co layer to prevent oxidation.) The Pt/Co layer was patterned into  $100 \times 100 \mu\text{m}^2$  pads. Cross-sectional transmission electron microscopy showed a sharp interface between the BFO and Co layers with no indication of Co oxide formation.

Longitudinal magneto-optical Kerr effect (MOKE) magnetic hysteresis loops were measured on a Co pad as the angle between the external magnetic field and the sample was swept. To increase the signal-to-noise ratio of the MOKE response, hysteresis loops from  $\geq 10$  measurements at each angle were averaged. From the angle-dependent hysteresis loops, the anisotropy axes were determined. The hysteresis loops of unpoled Co/BFO films with the magnetic field applied along the Co layer's magnetic easy and hard axes indicated uniaxial anisotropy in the Co layer, induced by exchange coupling between the Co and BFO layers [Fig. 5(a)]. Consistent with previous results,<sup>5</sup> the easy axis was along the  $[010]$  direction and had a unidirectional exchange bias field ( $H_E$ ) of  $\sim 4$  Oe.

Angle-dependent hysteresis loops were measured for unpoled, positive, and negative ferroelectric states (in that order), where the angle was defined between the applied field ( $H$ ) and the  $[010]$  direction of BFO ( $0^\circ$  and  $90^\circ$  correspond to the  $[010]$  and  $[100]$  directions, respectively). The angular dependencies of the saturation field ( $H_S$ ), the remanent ratio ( $M_R/M_S$ ), and  $H_E$  were extracted from the hysteresis loops [Figs. 5(b)–5(d), respectively].  $H_S$  along the easy axis was unaffected by the poling state, but differences near the hard axis were noticeable.  $H_S$  increased significantly with positive poling and decreased with negative poling. Interestingly, poling results changed the maxima of  $H_S$  (in the hard direction near  $270^\circ$ ). Similar behavior was observed for  $M_R/M_S$ : The ratios differed after poling.  $H_E$  clearly decreased with poling; the values for the  $+200$  and  $-200$  kV/cm poling states were similar. Thus, the applied electric field shifted exchange bias.

The magnetic moments associated with a given  $k$  domain in single-crystal BFO lie in the plane determined by the ferroelectric polarization and the propagation vector.<sup>15</sup> In addition, the projections of these moments into the plane containing the Co moments lie along the  $[100]$ ,  $[010]$ , and  $[110]$  directions for  $k_1$ ,  $k_2$ , and  $k_3$  magnetic domains. These were the easy axes found for the soft CoFeB layer deposited on single crystals in a previous study. This is also consistent

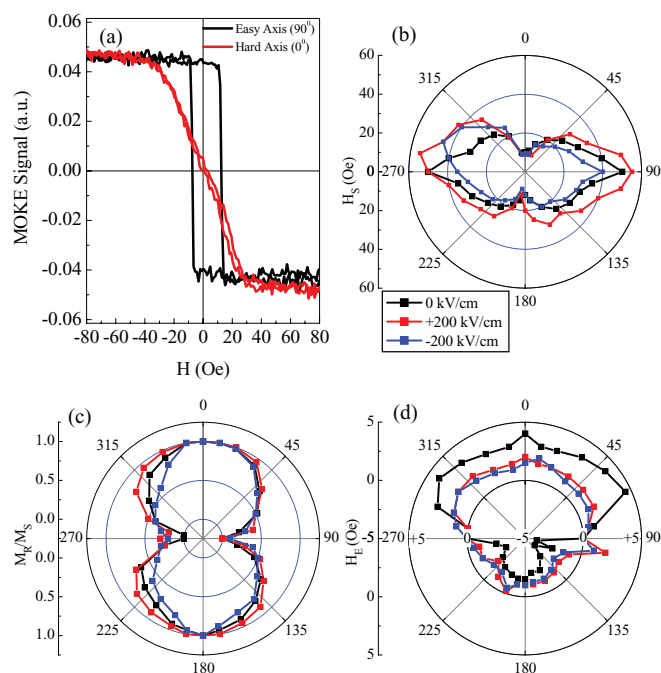


FIG. 5. (Color online) (a) Longitudinal MOKE loops of Co on BFO (unpoled). (b)–(d) Angular dependencies of  $H_S$ ,  $M_R/M_S$ , and  $H_E$  of Co on BFO. The inserted numbers in (d) refer to the exchange bias  $H_E$ .

with the easy axis we find in the present experiment. Thus, the projection of the cycloid into the Co plane sets the easy axis of these materials. From single-crystal measurements, only two  $k$  domains are typically observed. Thus, by changing their relative populations, we can control the projection of the net moments onto the Co film and thus determine its easy axis. For our films where the AFM moments form a

spiral structure, the easy axis did not change with electric-field application, whereas  $H_S$  did, suggesting that the relative domain populations did not shift enough to significantly change the easy and hard axes. Thus, the present tunable exchange bias is a one-way effect, where we could modify the exchange bias with the electric field—but only once. A similar conclusion was reached with films of different thicknesses and device geometry.<sup>21</sup> This suggests that spirals cannot be used to reproducibly change the easy axis in such systems.

We showed that magnetic domain populations in modulated BFO films changed upon electric-field application. Furthermore, when we deposited Co on such films, they exhibited exchange bias that can be shifted by application of electric field. The saturation field of such structures could also be changed by field application. Although we could not switch the easy axis of the Co layer, these results represent a major step toward understanding the mechanism of tunable exchange bias, with the ultimate goal of scalable, room-temperature magnetoelectric thin-film BFO devices. Recent works using different approaches show some promise.<sup>22</sup>

We acknowledge useful contributions from K. Kothapalli. We also acknowledge useful conversations with Mark Stiles and J. A. Borchers. Work at Maryland was supported by access to the Shared Experimental Facilities of the UMD-NSF-MRSEC (DMR 0520471), NSF DMR 0603644, and ARO W911NF-07-1-0410. The work was also supported by the W. M. Keck Foundation. The research at the High Flux Isotope Reactor, Oak Ridge National Laboratory was supported by the Scientific User Facilities Division, Office of Basic Energy Sciences, US Department of Energy. We acknowledge the support of the National Institute of Standards and Technology, US Department of Commerce through Grant No. 70NANB7H6177 and in providing neutron research facilities used in this work.

\*william.ratcliff@nist.gov

†Present address: Portland Technology Development, Intel Corporation, Hillsboro, OR 97124.

<sup>1</sup>T. Zhao, A. Scholl, F. Zavaliche, K. Lee, M. Barry, A. Doran, M. P. Cruz, Y. H. Chu, C. Ederer, N. A. Spaldin, R. R. Das, D. M. Kim, S. H. Baek, C. B. Eom, and R. Ramesh, *Nature Mater.* **5**, 823 (2006).

<sup>2</sup>H. Bea, M. Gajek, M. Bibes, and A. Barthelémy, *J. Phys.: Condens. Matter* **20**, 434221 (2008).

<sup>3</sup>Y.-H. Chu, L. W. Martin, M. B. Holcomb, M. Gajek, S.-J. Han, Q. He, N. Balke, C.-H. Yang, D. Lee, W. Hu, Q. Zhan, P.-L. Yang, A. Fraile-Rodriguez, A. Scholl, S. X. Wang, and R. Ramesh, *Nature Mater.* **7**, 478 (2008).

<sup>4</sup>L. W. Martin, Y.-H. Chu, M. B. Holcomb, M. Huijben, P. Yu, S.-J. Han, D. Lee, S. X. Wang, and R. Ramesh, *Nano Lett.* **8**, 2050 (2008).

<sup>5</sup>D. Lebeugle, A. Mougin, M. Viret, D. Colson, J. Allibe, H. Bea, E. Jacquet, C. Deranlot, M. Bibes, and A. Barthelémy, *Phys. Rev. B* **81**, 134411 (2010); D. Lebeugle, A. Mougin, M. Viret, D. Colson, and L. Ranno, *Phys. Rev. Lett.* **103**, 257601 (2009).

<sup>6</sup>S. Lee, W. Ratcliff II, S. W. Cheong, and V. Kiryukhin, *Appl. Phys. Lett.* **92**, 192906 (2008).

<sup>7</sup>D. Lebeugle, D. Colson, A. Forget, M. Viret, A. M. Bataille, and A. Goukasov, *Phys. Rev. Lett.* **100**, 227602 (2008).

<sup>8</sup>H. Bea, M. Bibes, F. Ott, B. Dupe, X. H. Zhu, S. Petit, S. Fusil, C. Deranlot, K. Bouzehouane, and A. Barthelémy, *Appl. Phys. Lett.* **93**, 072901 (2008).

<sup>9</sup>W. Ratcliff II, D. Kan, W. Chen, S. Watson, S. Chi, R. Erwin, G. J. McIntyre, S. C. Capelli, and I. Takeuchi, *Adv. Funct. Mater.* **21**, 1567 (2011).

<sup>10</sup>X. Ke, P. P. Zhang, S. H. Baek, J. Zarestky, W. Tian, and C. B. Eom, *Phys. Rev. B* **82**, 134448 (2010).

<sup>11</sup>Y.-H. Chu, M. P. Cruz, C.-H. Yang, L. W. Martin, P.-L. Yang, J.-X. Zhang, K. Lee, P. Yu, L.-Q. Chen, and R. Ramesh, *Adv. Mater.* **19**, 2662 (2007).

<sup>12</sup>B. C. Chakoumakos, H. Cao, F. Ye, A. D. Stoica, M. Popovici, M. Sundaram, W. Zhou, J. S. Hicks, G. W. Lynn, and R. A. Riedel, *J. Appl. Cryst.* **44**, 665 (2011).

<sup>13</sup>J. Wang, J. B. Neaton, H. Zheng, V. Nagarajan, S. B. Ogale, B. Liu, D. Viehland, V. Vaithyanathan, D. G. Schlom, U. V. Waghmare, N. A. Spaldin, K. M. Rabe, M. Wuttig, and R. Ramesh, *Science* **299**, 1719 (2003).

- <sup>14</sup>S. Lee, T. Choi, W. Ratcliff II, R. Erwin, S.-W. Cheong, and V. Kiryukhin, *Phys. Rev. B* **78**, 100101 (2008).
- <sup>15</sup>I. Sonowska, T. Peterlin-Neumaier, and E. Steichele, *J. Phys. C* **15**, 4835 (1982).
- <sup>16</sup>Tapan Chatterji, *Neutron Scattering from Magnetic Materials* (Elsevier, Amsterdam, 2006).
- <sup>17</sup>Claude Ederer and Nicola A. Spaldin, *Phys. Rev. B* **71**, 060401 (2005).
- <sup>18</sup>J. A. Vrugt, C. J. F. ter Braak, C. G. H. Diks, B. A. Robinson, J. M. Hyman, and D. Higdon, *Int. J. Nonlinear Sci. Numer. Simul.* **10**, 273 (2009).
- <sup>19</sup>S. M. Wu, Shane A. Cybart, P. Yu, M. D. Rossell, J. X. Zhang, R. Ramesh, and R. C. Dynes, *Nature Mater.* **9**, 756 (2010); J. T. Heron, M. Trassin, K. Ashraf, M. Gajek, Q. He, S. Y. Yang, D. E. Nikonov, Y.-H. Chu, S. Salahuddin, and R. Ramesh, *Phys. Rev. Lett.* **107**, 217202 (2011).
- <sup>20</sup>Julie Allibe, Stephane Fusil, Karim Bouzehouane, Christophe Daumont, Daniel Sando, Eric Jacquet, Cyrille Deranlot, Manuel Bibes, and Agnes Barthelemy, *Nano Lett.* **12**, 1141 (2012).
- <sup>21</sup>Any mention of commercial products within this paper is for information only; it does not imply recommendation or endorsement by NIST.
- <sup>22</sup>Xi He, Yi Wang, Ning Wu, Anthony N. Caruso, Elio Vescovo, Kirill D. Belashchenko, Peter A. Dowben, and Christian Binek, *Nature Mater.* **9**, 579 (2010); Ming Liu, Jing Lou, Shandong Li, and Nian X. Sun, *Adv. Funct. Mater.* **21**, 2593 (2011); S. M. Wu, Shane A. Cybart, D. Yi, James M. Parker, R. Ramesh, and R. C. Dynes, *Phys. Rev. Lett.* **110**, 067202 (2013).